Unveiling layer-dependent interlayer coupling and vibrational properties in $MoTe_2$ under high pressure

Xing Xie,[1,2,*] Junnan Ding,[1,2,*] Biao Wu,[1,2] Haihong Zheng,[1,2] Shaofei Li,[1] Jun He,[1] Zongwen Liu,[3,4] Jian-Tao Wang,[5,6,7] and Yanping Liu[1,2,8,†]

[1]*Institute of Quantum Physics, School of Physics, Central South University, 932 South Lushan Road, Changsha, Hunan 410083, People's Republic of China*

[2]*State Key Laboratory of High-Performance Complex Manufacturing, Central South University, 932 South Lushan Road, Changsha, Hunan 410083, People's Republic of China*

[3]*School of Chemical and Biomolecular Engineering, The University of Sydney, NSW 2006, Australia*

[4]*The University of Sydney Nano Institute, The University of Sydney, NSW 2006 Australia*

[5]*Beijing National Laboratory for Condensed Matter Physics, Institute of Physics, Chinese Academy of Sciences, Beijing 100190, People's Republic of China*

[6]*School of Physical Sciences, University of Chinese Academy of Sciences, Beijing 100049, People's Republic of China*

[7]*Songshan Lake Materials Laboratory, Dongguan, Guangdong 523808, People's Republic of China*

[8]*Shenzhen Research Institute of Central South University, Shenzhen 518000, People's Republic of China*

(Received 27 June 2023; revised 22 September 2023; accepted 28 September 2023; published 12 October 2023)

Layered materials have garnered significant attention for their ability to exhibit tunable physical properties through stacking, twisted angles, and interlayer coupling. The interlayer vibrations in these materials are highly sensitive to, and can be controlled by, their thickness. However, the layer-dependent interlayer vibration behavior under high pressure remains unclear. Here, we investigate the layer-dependent high-pressure Raman spectroscopy of 1–5L and bulk $MoTe_2$ up to 14-GPa pressure, and demonstrate a pressure-induced thickness-dependent interlayer vibration behavior. We observe the pressure-induced blueshift rates of the breathing (LB) and shear (S) modes exhibit opposite strong layer-dependent behaviors, which arise from thickness-dependent interlayer coupling and restoring forces, respectively. Furthermore, we propose a pressure-dependent linear chain model to characterize the force constants under pressure and employ a bond-polarization model to explain the intensity changeover between the S and LB modes, as well as between the A_1'/A_{1g}^2 and $E'/E_g{}^1$ modes, which is attributed to the increase in interlayer Te–Te bond angle and intralayer distance between Mo and Te atomic layers, respectively. Our findings elucidate the robust thickness-dependent interlayer vibrations in $MoTe_2$ and provide a firm foundation for exploring and characterizing interlayer coupling through pressure engineering in van der Waals materials.

DOI: 10.1103/PhysRevB.108.155302

I. INTRODUCTION

Layered materials, such as graphene [1], black phosphorus [2], and transition-metal chalcogenides (TMDs) [3], exhibit a unique crystal structure characterized by van der Waals interactions between layers. This distinctive structure imparts them with remarkable properties, including high carrier mobility [4], extraordinary optoelectronic properties [5,6] and layer-dependent band gaps [7,8], making them highly valuable in various applications such as optoelectronic detector [9], spintronic [10], valley optoelectronics [11], and field-effect transistors [12]. In particular, such structural features enable flexible tuning of their properties through methods such as stacking [13], twisted angle [14–17], and the application of external field [18–20]. Current research efforts have extensively explored structural transition [21,22], semiconductor-to-metal transition [23,24], optical transition changeover [25,26], and pressure-induced superconductor [27,28] in layered materials and their heterostructures, accomplished by adjusting the interlayer coupling through high pressure. The high-pressure studies for two-dimensional (2D) materials have been focused on their monolayer [29], bilayers [30], heterostructures [31], and bulk [32]. However, there is a lack of systematic high-pressure studies on 2D materials with varying layer numbers. In TMDs, the low-frequency interlayer vibration modes are highly sensitive to the number of layers [33–35], resulting in blue- and redshifts for shear (S) and breathing (LB) modes, respectively, as the thickness increases. The description of these low-frequency S and LB modes can be achieved using the linear chain model (LCM) [36,37], and their layer-dependent behavior can be characterized by a fan diagram [33]. Given that the S and LB modes are closely related to interlayer interactions, pressure can effectively modulate these modes by controlling the interlayer coupling. However, the response of S and LB modes in 2D

*These authors contributed equally to this work.
†liuyanping@csu.edu.cn

materials with different thicknesses under pressure remains poorly understood.

In this work, we performed high-pressure Raman spectroscopy studies on monolayer (1L) to pentalayer (5L) and bulk $MoTe_2$ using diamond-anvil cell (DAC) devices. The obtained high-pressure Raman spectra revealed that the blueshift ratio of the S and LB modes is dependent on the layer number, exhibiting contrasting trends due to the layer-dependent restoring force and interlayer coupling, respectively. Moreover, we extended the LCM to the pressure field and obtained a continuous increase in the force constants of the S and LB modes with increasing pressure. Additionally, we uncovered a pressure-induced intensity changeover between the S and LB modes, as well as between A_1'/A_{1g}^2 and E'/E_g^1 modes. By employing the bond-polarization model, we identified that this intensity changeover arises from pressure-induced alterations in the polarization component of the interlayer Te–Te or intralayer Mo–Te bonds. Our study provides insights into the layer-dependent atomic vibrations and their responses under high pressure.

II. METHODS

A. Sample preparation

The layer-dependent samples used in this study were prepared through gold-assisted mechanical exfoliation [38,39] from bulk $MoTe_2$ crystals grown by flux-zone growth (Flux) implemented by the 2D Semiconductors company. A layer of 130–140-nm-thick gold was deposited onto the bulk $MoTe_2$ samples by a vacuum thermal evaporation device. Subsequently, thermal release tape was employed to adhere these gold films, and then obtain the few-layer (1–5 L) samples using potassium iodide solution (KI:I_2:deionized water = 4 g:0.5 g:40 g) to etch the gold layer. In order to conduct high-pressure experiments, these samples were transferred from Si/SiO_2 substrates to the DAC culets using a dry-transfer method [40,41] with transfer medium of Polycarbonate (PC) glue. We dripped PC glue onto polydimethylsiloxane stuck on a glass slide, and then heated the Si/SiO_2 substrate to $80^\circ - 90^\circ$ C temperature. Upon cooling to room temperature, the $MoTe_2$ samples were picked up. Afterward, the samples attached to PC glue were heated to $90^\circ - 100^\circ$ C temperature, enabling the release of these samples with PC glue onto culets of DAC. The PC glue was removed using chloroform solution. To protect the $MoTe_2$ samples and ensure good optical coupling, a multilayer hBN was applied on top of the samples. Finally, a 140-nm-thick gold film was deposited on the samples for enhanced optical reflectivity during the measurements.

B. High-pressure optical measurements

The Raman spectra of the $MoTe_2$ samples were acquired using the WITec Alpha 300R system equipped with a continuous wave (cw) laser (532 nm). Raman measurements were performed using an optical grating with a line density of 1800 lines per millimeter and a 50× objective with the focal length of 3.6 mm, the work distance of 10.6 mm, and numerical aperture of 0.5. The Raman scattered light was detected by a charge-coupled device with an integration time of 5 s and accumulation of 7 at a laser power of 15 mW. The laser beam size was ∼1 μm. To generate high pressure, a DAC with a 400-μm culet size was employed. Pressure was controlled by using silicone oil as a pressure-transmitting medium, and the pressure values were calibrated using ruby granules as a pressure calibration standard [42]. By continuously adjusting the applied pressure, high-pressure Raman spectra were collected to investigate the pressure-dependent behavior of the samples.

C. Theoretical calculations

Density-functional theory (DFT) calculations were performed using the projector augmented-wave [43] method, implemented in the Vienna *Ab initio* Simulation Package (VASP) code [44]. The Perdew-Burke-Ernzerhof [45] exchange-correlation functional within the generalized gradient approximation was employed. A plane-wave energy cutoff of 520 eV and a k-point mesh of $13 \times 13 \times 1$ were used for the calculations. To avoid the interactions between periodic layers, a vacuum spacing of 20 Å was included. The crystal structure of bulk $MoTe_2$ was relaxed until the forces converged to within 0.01 eV/Å under both zero-pressure and high-pressure conditions.

III. RESULTS AND DISCUSSION

A. Low-frequency Raman spectra at ambient pressure

Bulk $MoTe_2$ crystallizes D_{6h}^4 symmetry, and has 12 irreducible representations at the Γ point [46,47]:

$$\Gamma_{\text{bulk}} = A_{1g} + 2A_{2u} + 2B_{2g} + E_{1g} + 2E_{1u} + E_{2u} + B_{1u} + 2E_{2g}, \quad (1)$$

where A_{1g}, E_{2g}^1, E_{2g}^2, and E_{1g} are Raman-active modes. As the thickness of $MoTe_2$ changes from bulk to few layers, the symmetry alters to D_{3h}^1 and D_{2d}^3 for odd- and even-number layers, respectively. Thus, the Raman-active modes become A_1', E', and E'' for odd-number layers and become A_{1g}^2, E_g^1, and E_g^2 for even-number layers corresponding to the A_{1g}, E_{2g}^1, and E_{1g} for bulk, respectively. To investigate the vibration features of $MoTe_2$ materials, the few-layer $MoTe_2$ samples were obtained by mechanically exfoliating bulk $MoTe_2$ crystals, as depicted in Fig. 1(b). Raman spectroscopy measurements were performed at room temperature and ambient pressure, as presented in Fig. 1(d). Two low-frequency modes ($< 100\,\text{cm}^{-1}$) were observed in the Raman spectra of 2–5L $MoTe_2$ and identified as the S and LB modes. Specifically, for 2L, 3L, 4L, and 5L $MoTe_2$, the S (LB) modes were observed at 19.0 (27.0), 23.5 (19.5), 24.0 (14.5), and 25.5 cm^{-1} (11.5 cm^{-1}), respectively. The S and LB modes exhibit nonlinear blue- and redshifts, respectively, as the layer number increases, with a crossing point between 2L and 3L, which is consistent with previous findings [35].

The S and LB modes arise from the relative motion of the layers along the in-plane and out-of-plane directions, respectively, in $MoTe_2$ with N layers ($N \geqslant 2$). Each layer can be considered as a rigid atomic plane, enabling the use of the LCM [33,36,37] to describe the interlayer displacements. The vibrational frequencies of the S and LB modes can be

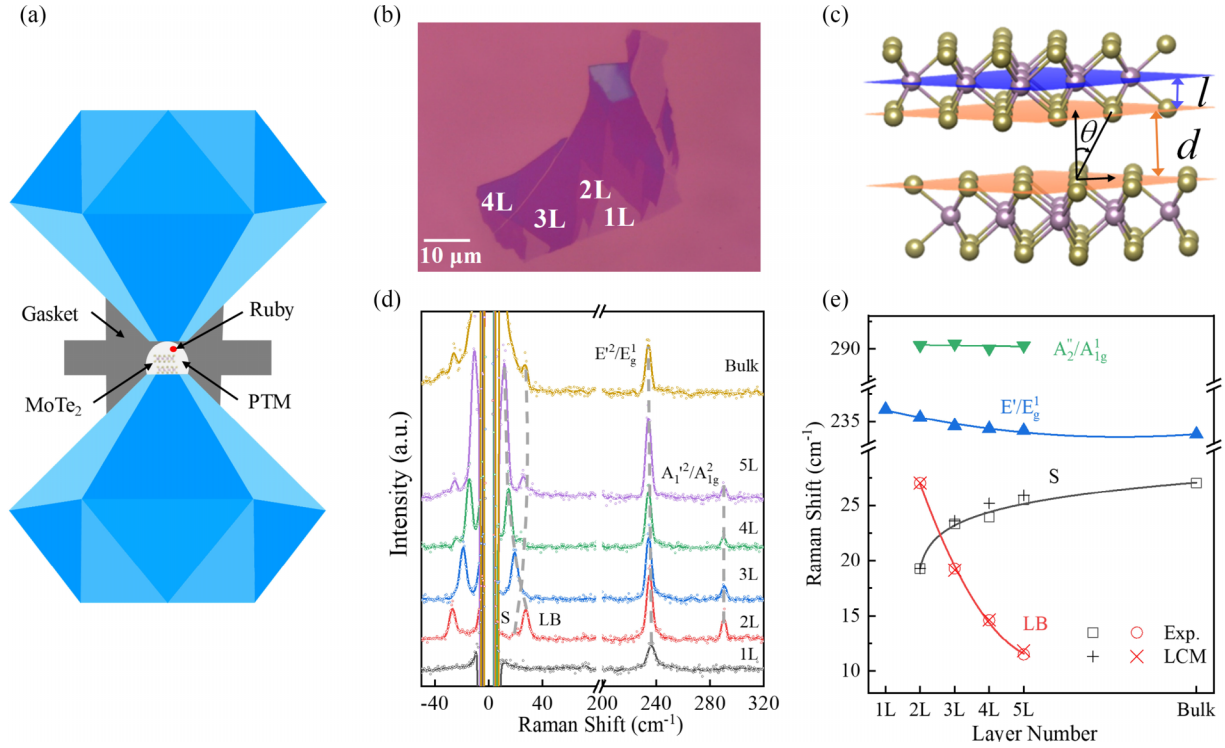

FIG. 1. Layer-dependent Raman spectra of $MoTe_2$ at ambient pressure. (a) Schematic diagram of diamond-anvil cell (DAC) device used for the experiments. (b) Optical image of few-layer $MoTe_2$ samples, including 1L, 2L, 3L, and 4L $MoTe_2$. (c) Crystal structure of $MoTe_2$, illustrating arrangement of Mo (lilac) and Te (yellowish-brown) atoms. Distances between adjacent Te atomic layers (interlayer) and between Mo and Te atomic layers (intralayer) are denoted as d and l, respectively. Angle (θ) is formed by adjacent interlayer Te–Te bonds and out-of-plane direction. (d) Raman spectra of $MoTe_2$ as function of layer number. Circle points and solid lines represent measured data and smoothing data (Loess method with window ratio of 0.008), respectively. (e) Layer-dependent Raman peak positions of $MoTe_2$. Low-frequency shear- and breathing modes exhibit blue- and redshifts, respectively, as layer number increases, consistent with results obtained from LCM.

described by the following equations:

$$\omega(S_{N,N-j}) = \frac{1}{\pi c}\sqrt{\frac{k_S}{M}}\sin\left(\frac{j\pi}{2N}\right)$$
$$\omega(LB_{N,N-j}) = \frac{1}{\pi c}\sqrt{\frac{k_{LB}}{M}}\sin\left(\frac{j\pi}{2N}\right), \quad (2)$$

where $M = m_{Mo} + 2m_{Te}$ is the total mass per unit cell, and c is the velocity of light. The j (index $j = 1, \ldots, N-1$) is equal to $N-1$ and 1 for the highest-frequency S modes and lowest-frequency LB modes, which can be observed in backscattering-configuration Raman spectra. We used the detected frequencies of S and LB modes of 2L $MoTe_2$ and the force constant of $k_S = 3.43 \times 10^{19}\,N/m^3$ and $k_{LB} = 6.88 \times 10^{19}\,N/m^3$ were obtained. The estimated results obtained from the LCM are in agreement with our measured results [see Fig. 1(e)]. Notably, these layer-dependent S and LB modes exhibit higher sensitivity to interlayer coupling compared to E'/E_g^1 and A_2''/A_{1g}^1 modes (E' and A_2'' for odd layer, while E_g^1 and A_{1g}^1 for even layer). This demonstrates the effectiveness of utilizing the interlayer S and LB modes as characterizations for studying interlayer coupling.

B. Positions of shear- and breathing modes at high pressure

To gain insight into the layer-dependent interlayer coupling in $MoTe_2$, we conducted compression experiments on $MoTe_2$ samples with varying layer numbers (2–5L and bulk) using DAC devices. Figure 2 illustrates the low-frequency Raman spectra as a function of pressure up to approximately 14 GPa. Due to the pressure-induced phonon-hardening effect, the S and LB modes of $MoTe_2$ exhibited monotonic blueshifts within the studied pressure range. Nevertheless, the low-frequency modes displayed a nonlinear behavior, characterized by a rapid variation at low pressures and a slower increase at high pressures. This nonlinear blueshift of the S and LB modes suggests distinct variations in interlayer coupling within different pressure ranges in $MoTe_2$ materials. To comprehend this nonlinear interlayer coupling variation, we carried out structure relaxation simulations on bulk $MoTe_2$ under pressures ranging from 0 to 14 GPa using first-principle calculations. Notably, the interlayer distance (d) showed a rapid decrease at low pressures (0–2-GPa range), followed by a gradual decrease at high pressures (2–14-GPa range), which aligns with our experimental findings [see Fig. 3(d)].

Furthermore, we plotted the frequency difference ($\Delta\omega = \omega_p - \omega_0$, where ω_p and ω_0 represent frequency at high pressure and at ambient pressure, respectively) between the pressure-dependent S and LB modes and the ambient-pressure S and LB modes as a function of pressure, as shown in Figs. 3(a) and 3(b), respectively. It was observed that for the LB modes, the blueshift rates decreased as the layer number increased. In contrast, for the S modes, thicker $MoTe_2$ samples exhibited a faster blueshift rate. To quantify these

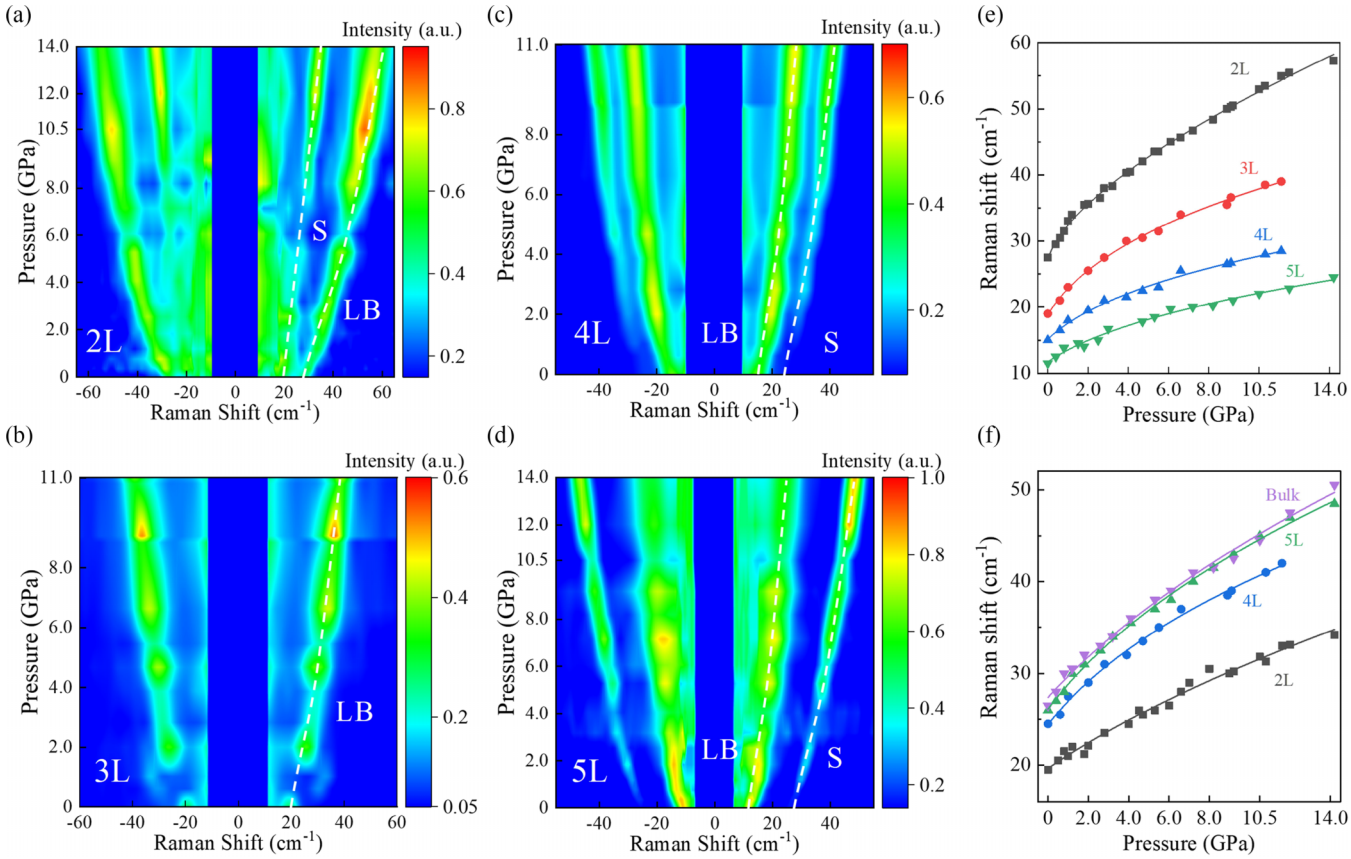

FIG. 2. Pressure-dependent low-frequency Raman spectra in layer-dependent $MoTe_2$. (a)–(c) Color plots depicting progressive changes in Raman spectra with increasing pressure for different layer thicknesses: (a) bilayer (2L) $MoTe_2$, (b) trilayer (3L) $MoTe_2$, (c) four layer (4L) $MoTe_2$, and (d) five layer (5L) $MoTe_2$. (e) Pressure-dependent variations in positions of the breathing (LB) modes. (f) Pressure-dependent variations in positions of shear (S) modes. All S and LB modes consistently exhibit blueshift as applied pressure intensifies.

observations, we fitted the measured data with a function of $\omega_N = A|p-xc|^{\alpha}$, where A and α are the amplitude and index, respectively. The fitted coefficients are listed in Table S1 of Supplemental Material (SM) [48]. Since the coefficient A predominantly controls the magnitude of the curves, we plotted the A coefficients as a function of layer number [Fig. 3(c)]. The A coefficients for the S and LB modes exhibited layer-dependent blue- and redshifts, respectively, as the layer number increased from 2L to 5L, consistent with the observed layer-dependent increase in blueshift rates for the S and LB modes under pressure. Additionally, a crossing point between the S and LB modes close to 4L suggests a small frequency difference between the S and LB modes in 4L $MoTe_2$ under pressure [Fig. 4(e)].

Simultaneously, the calculated d for 2–5L $MoTe_2$ (see Fig. 3(d) and SM Table S1 [48]) indicate an increase in interlayer coupling as the layer number increases from 2L to 5L. Thicker $MoTe_2$ samples exhibit stronger interlayer coupling, leading to a more moderate response to pressure, as observed in the pressure-dependent LB modes of $MoTe_2$ with different layer numbers. This is because structures with strong coupling exhibit greater resistance to external fields. The calculated interlayer distances, which show reduced variation rates under pressure, provide compelling evidence for the fact that strong interlayer coupling exhibits strong resistance to compression [Fig. 3(d)]. This finding also suggests that the LB modes of $MoTe_2$ are strongly influenced by interlayer coupling. As depicted in Fig. 3(e), external pressure narrows the interlayer distance and enhances interlayer coupling. Therefore, the use of a DAC provides an effective means to tune interlayer coupling, with LB modes offering a direct means of detecting interlayer coupling.

In contrast, the entire restoring force [36] also makes a significant contribution to the S modes of $MoTe_2$, in addition to interlayer coupling. In fact, due to enhanced surface binding, the overall restoring force increases with increasing thickness, resulting in a blueshift of the S modes in Bernal-stacked graphene [36]. This trend of S-mode hardening with increasing layer number was also observed in our experimental data for $MoTe_2$ [Fig. 1(e)]. This thickness-dependent surface binding leads to an increase in the pressure-induced blueshift rate with increasing layer number. When high pressure is applied, the interlayer distance decreases, along with an increase in θ [see Fig. 4(d)], thereby enhancing interlayer coupling and surface binding. Thus, under the combined effects of enhanced interlayer coupling and overall restoring force, the S modes exhibit a pressure-induced blueshift.

Given the suitability of the rigid atomic plane assumption for NL $MoTe_2$(N = 2−5) under pressure, we employed the pressure-dependent LCM (p-LCM) to estimate the pressure-dependent force constant and understand the variation in interlayer coupling under pressure. It should be noted that

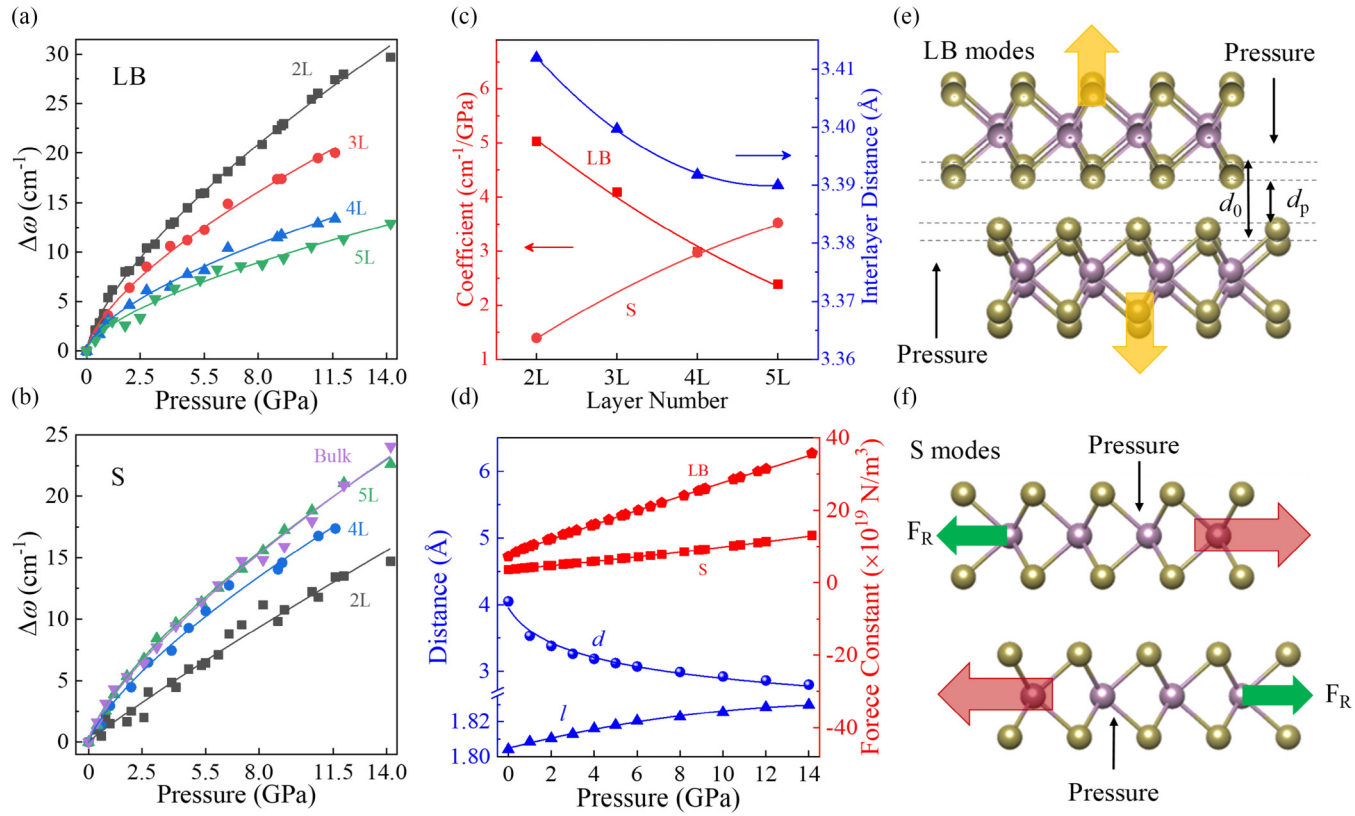

FIG. 3. Layer-dependent peak positions of S and LB modes in $MoTe_2$ under pressure. (a), (b) Normalized Raman peak positions of (a) LB and (b) S modes with different thickness as function of pressure, relative to peak position at ambient pressure. Values are denoted as $\Delta\omega = \omega_p - \omega_0$, where ω_p and ω_0 are frequencies of LB and S modes at high pressure and ambient pressure, respectively. (c) Layer-dependent calculated interlayer distance (blue line) and coefficients A for S and LB modes (red lines). (d) Pressure-dependent force constant calculated from p-LCM (red lines) and calculated interlayer (d) and intralayer (l) spacing distances of bulk $MoTe_2$ (blue lines). (e), (f) Vibration patterns of (e) LB and (f) S modes. F_R denotes restoring force.

the mass M varies with pressure due to the pressure-induced lattice reduction. The p-LCM can be expressed as follows:

$$\omega_p(S_{N,N-j,p}) = \frac{1}{\pi c}\sqrt{\frac{k_{\mathrm{S,p}}}{M_p}}\sin\left(\frac{j\pi}{2N}\right)$$
$$\omega_p(LB_{N,N-j,p}) = \frac{1}{\pi c}\sqrt{\frac{k_{\mathrm{LB,p}}}{M_p}}\sin\left(\frac{j\pi}{2N}\right). \quad (3)$$

Here, we adopted the calculated mass M_p of bulk $MoTe_2$ under pressure (see Fig. S3 [48]). Using our measured pressure-dependent frequencies of S and LB modes [$\omega_p(S_{2,1,p})$ and $\omega_p(LB_{2,1,p})$], we estimated the force constants $k_{\mathrm{S},p}$ and $k_{\mathrm{LB},p}$, as illustrated in Fig. 3(d). The estimated pressure-dependent LB modes for NL $MoTe_2$ ($N = 3$, 4, and 5) closely matched the experimental data [Fig. 4(a)], confirming the feasibility of p-LCM for the LB modes of NL $MoTe_2$. Clearly, both $k_{\mathrm{S},p}$ and $k_{\mathrm{LB},p}$ exhibit a blueshift as high pressure was applied, with $k_{\mathrm{LB},p}$ being more sensitive to pressure than $k_{\mathrm{S},p}$. This implies that the strength of interlayer coupling of NL $MoTe_2$ was enhanced by high pressure, and the layer-dependent low-frequency modes at high pressure exhibited similar behavior to those at ambient pressure (i.e., pressure did not change the layer-dependent characteristic of the low-frequency Raman modes).

C. Intensity of low-frequency Raman spectra

In terms of the intensity of the S and LB modes, we observed that the intensity of the S modes was enhanced by pressure relative to the LB modes at corresponding pressures. We extracted the intensity of S and LB modes of 2L, 4L, and 5L $MoTe_2$ under pressure and plotted their ratio (I_S/I_{LB}) as a function of pressure, as shown in Fig. 4(c). It exhibits a distinct upward trend for NL $MoTe_2$ ($N = 2$, 4, and 5), especially for 4L and 5L $MoTe_2$, which display a nearly linear increase. At approximately 10-GPa pressure, the I_S/I_{LB} ratio reaches 1 for 4L and 5L $MoTe_2$. To gain insight into the physics underlying the pressure-induced enhancement of I_S/I_{LB}, we employed the empirical bond-polarizability model [49–51]. The Raman intensity can be described according to the Placzek approximation [51,52]:

$$I(k) \propto \frac{n_k+1}{\omega_k}\left|\boldsymbol{e}_i\cdot\widetilde{R}(k)\cdot\boldsymbol{e}_s^T\right|^2$$
$$= \frac{n_k+1}{\omega_k}\left|\sum_{\mu\nu} e_{i,\mu}e_{s,\nu}\Delta\alpha_{\mu\nu}(k)\right|^2, \quad (4)$$

where $\widetilde{R}(k)$ and ω_k are the Raman tensor and frequency of phonon mode k, respectively. $\boldsymbol{e}_i$ and $\boldsymbol{e}_s$ are the polarization vector of incident and scattered light, and the μ and ν de-

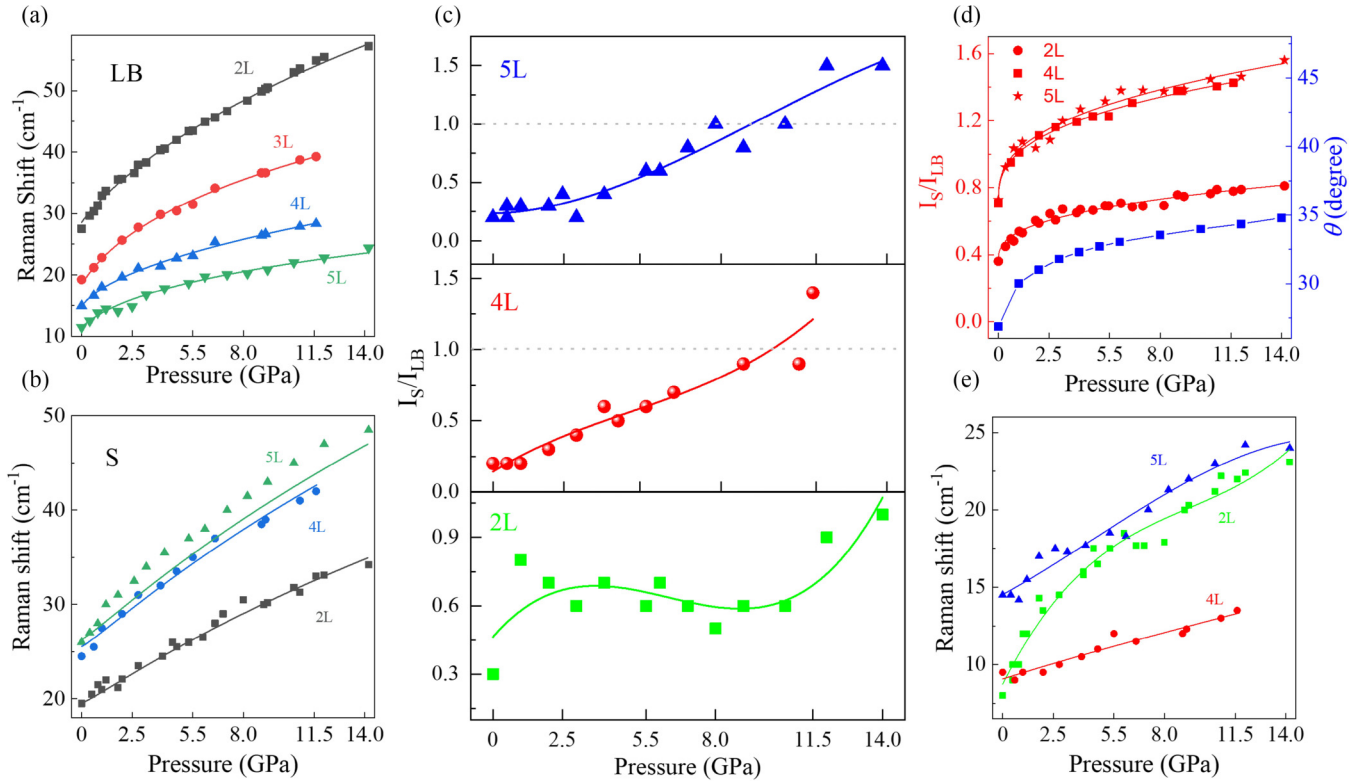

FIG. 4. Pressure-induced intensity changeover between S and LB modes of $MoTe_2$. (a), (b) Raman peak position of (a) LB and (b) S modes of few-layer $MoTe_2$. Points represent measured data, while lines denote simulated results of p-LCM. (c) Intensity ratio between S and LB modes (I_S/I_{LB}) of 2L (green), 4L (red), and 5L (blue) $MoTe_2$. Lines are provided as visual guides. (d) Calculated pressure-dependent angle (θ) by first-principle calculations (blue curves) and estimated I_S/I_{LB} of 2L, 4L, and 5L $MoTe_2$ by bond-polarization model (red curves). (e) Frequency difference between LB and S modes of 2L, 4L, and 5L $MoTe_2$ as function of pressure.

note components of the tensor, respectively. Moreover, n_k is the phonon occupancy, which can be determined using Bose-Einstein statistics [$n_k = 1/(e^{\hbar\omega_k/k_BT} - 1)$]. According to the bond-polarizability model, the Raman tensor elements $\Delta\alpha_{\mu\nu}(k)$ have the following forms [51]:

$$\Delta\alpha_{xx,\mu}(k) = \sum_i \sum_B C_{i\mu,B}\widehat{R}_{i\mu,B}\Delta r_{i\mu}. \tag{5}$$

Here, $C_{i\mu,B}$, $\widehat{R}_{i\mu,B}$, and $\Delta r_{i\mu}$ are the coefficients, normalized bond vector, and atomic displacement of μ component for bond B connected to atom i, respectively. The subscript xx represents the backscattering configuration $\widetilde{z}(xx)z$. For the S modes, the bond B has the x or y component, whereas the B is along the z component for LB modes. Therefore, the I_S/I_{LB} can be expressed as

$$\frac{I_S}{I_{LB}} \propto \frac{\omega_{LB}}{\omega_S}\left|\frac{\Delta\alpha_{xx,x}(\omega_S)}{\Delta\alpha_{xx,z}(\omega_{LB})}\right|^2. \tag{6}$$

Based on the analysis of Liang *et al.* [51] for TMDs, the Raman tensor elements are $\sqrt{2}C_{x,B}\sin\theta$, $3C_{x,B}\sin\theta$, and $\frac{8}{5}\sqrt{5}C_{x,B}\sin\theta$ [θ is the angle formed by adjacent interlayer Te–Te bond and out-of-plane direction; see Fig. 1(c)] for S modes of 2L, 4L, and 5L $MoTe_2$, respectively, while $\sqrt{2}C_{z,B}\cos\theta$ for LB modes of 2L, 4L, and 5L $MoTe_2$ within normalized layer displacements (where $C_{x,B} = C_{z,B}$). Note that the calculated pressure-dependent θ of bulk $MoTe_2$ was adopted [Fig. 4(d)].

Figure 4(d) shows the estimated I_S/I_{LB} ratios for 2L, 4L, and 5L $MoTe_2$ using Eq. (6). These ratios increase with increasing pressure, aligning with the observed upward trend in the experimental data. This suggests that the θ, which is correlated with the interlayer distance and interlayer slipping, can affect the intensity of the S and LB modes by changing their bond polarization. As a result, pressure induces an intensity changeover between the S and LB modes in $MoTe_2$.

D. High-frequency Raman spectra

Regarding the high-frequency Raman spectra of 1L $MoTe_2$ and bulk $MoTe_2$, we observed Raman peak of $A_1'(A_{1g})$ and $E'(E^1_{2g})$ at 171.5 (173.5) cm^{-1} and 236.0 (234.0) cm^{-1} for 1L (bulk) $MoTe_2$ at ambient pressure (see Figs. S1 and S2 of SM [48]), which are consistent with the previous results [35,46,53–55]. In NL $MoTe_2$ ($N = 2$, 3, 4, and 5), an additional infrared-active peak located around 290 cm^{-1} (A_2''/A^1_{1g}) [35,47] was detected at ambient pressure, as shown in Fig. 5(a) and Fig. S1 and Fig. S2 in SM [48]. All high-frequency Raman modes exhibited a monotonic blueshift under pressure. For bulk $MoTe_2$, the A_{1g} and E^1_{2g} modes displayed different increasing tendencies in the pressure range of 0–7.0 GPa and 8.0–14.0 GPa, respectively, implying a transition from semiconductor phase to metal phase in the

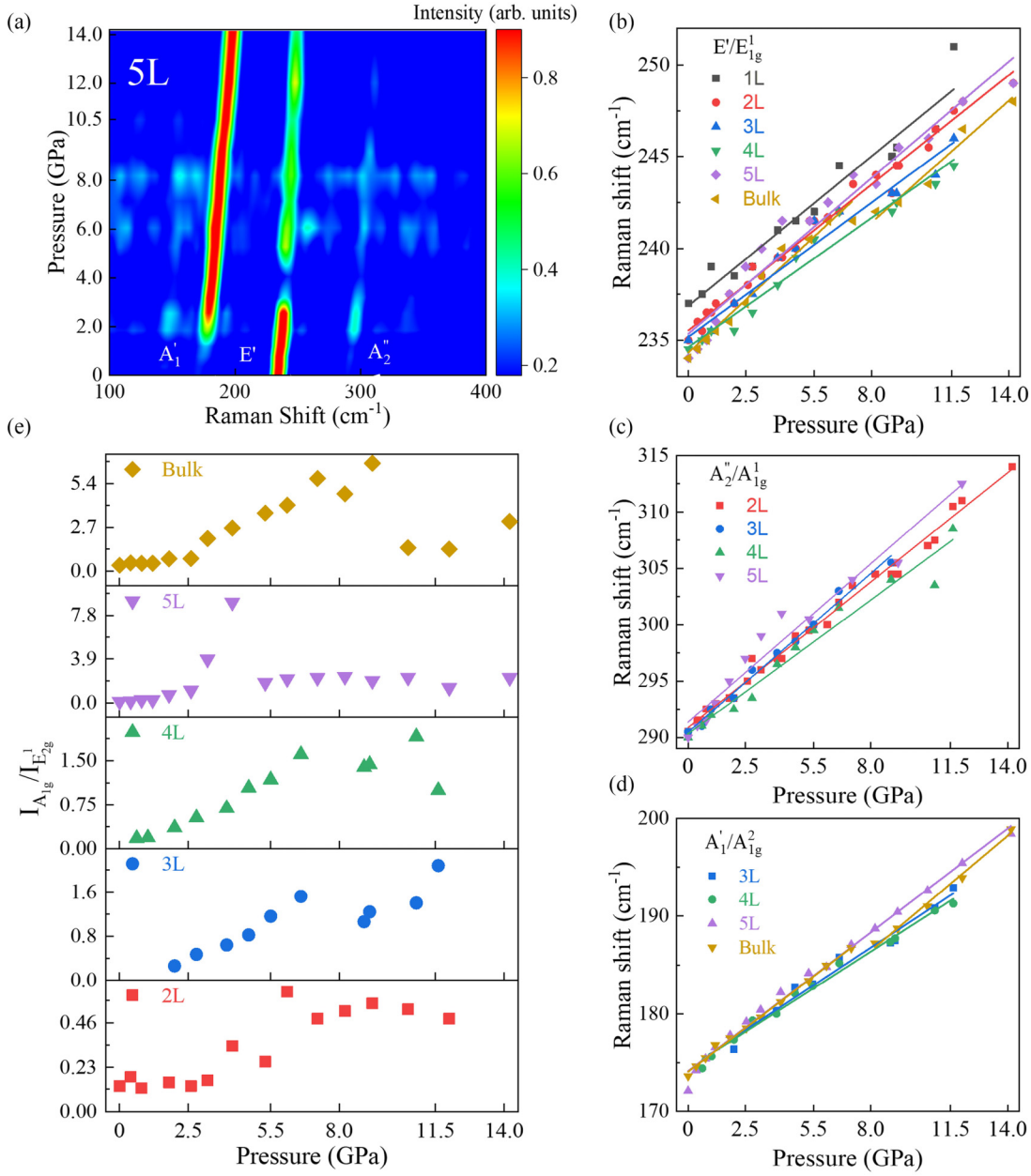

FIG. 5. High-frequency Raman spectra of $MoTe_2$ under pressure. (a) Pressure-dependent Raman spectra of 5L $MoTe_2$ in wave-number range of $100 - 400\,cm^{-1}$. (b)–(d) Pressure evolution of high-frequency Raman peak positions for (b) E'/E^1_g, (c) A_2''/A^1_{1g}, and (d) A_1'/A^2_{1g} modes. Experimental data points were extracted from Raman spectra, and solid curves represent fitted results for visual guidance. All of these vibration modes exhibit a blueshift with increasing pressure. (e) Intensity ratio between A_1'/A^2_{1g} and E'/E^1_g modes ($I_{A_{1g}}/I_{E^1_{2g}}$) for 2–5 L and bulk $MoTe_2$, showing an increasing trend with increasing pressure.

pressure range of 7.0–8.0 GPa. This semiconductor-to-metal transition and its transition pressure were in agreement with the previous results, with a transition pressure at around 10 GPa [55].

Moreover, the pressure-dependent high-frequency Raman positions showed little dependence on the layer number [see Figs. 5(b)–5(d)], even though the E'/E^1_g modes decreased with increasing layer number [Fig. 1(e)]. This is in contrast to the low-frequency S and LB modes in $MoTe_2$, suggesting that intralayer vibrations are not significantly influenced by the layer number under pressure. As the stacking layers and pressure increase, the variation in intralayer atomic vibration is small, indicating that the intralayer Te-Mo-Te configuration does not exhibit large differences between different layers due to the strong Mo–Te covalent bond, which provides significant resistance to strain.

However, their intensity can be tuned by the high pressure. We plotted the intensity ratio between A_1'/A^2_{1g} and E'/E^1_g modes ($I_{A_{1g}}/I_{E^1_{2g}}$) for 2–5L and bulk $MoTe_2$, as shown in Fig. 5(e). As the pressure increased, $I_{A_{1g}}/I_{E^1_{2g}}$ displayed an upward trend and showed a layer-dependent behavior (more thickness of $MoTe_2$ has higher $I_{A_{1g}}/I_{E^1_{2g}}$). To understand

the pressure-induced $I_{A_{1g}}/\ I_{E^1_{2g}}$ enhancement, we performed first-principle calculations of intralayer atomic and crystal relaxation for bulk $MoTe_2$ under pressure. Figure 3(d) illustrates the increasing intralayer distance between Mo and Te atomic layers (l) with increasing the pressure, resulting from enhanced Coulomb repulsion under pressure. Consequently, the increase in l leads to an increase in the out-of-plane component and a decrease in the in-plane component of Te–Mo bond. According to the bond-polarization model [Eq. (4)], the intensity of phonon vibration modes is related to the bond-polarization component. Thus, the $I_{A_{1g}}/\ I_{E^1_{2g}}$ can be enhanced when pressure increases the l.

Furthermore, we investigated the pressure evolution of the wave-number difference between A and E modes ($A_2^{''} - E'/A^1_{1g} - E^1_{1g}$ and $E' - A_1{}'/E^1_{1g} - A^2_{1g}$) in $MoTe_2$. For $A_2^{''} - E'/A^1_{1g} - E^1_{1g}$, they exhibited blueshift and could be fitted with a linear trend (see Fig. S4 in SM [48]), indicating the gradual enlargement of the gaps between $A_2^{''}$ and E'(or A^1_{1g} and E^1_{1g}) for 2–5L $MoTe_2$. In contrary, the wave-number difference $E' - A_1{}'/E^1_{1g} - A^2_{1g}$ declined with increasing pressure for 3–5 L and bulk $MoTe_2$, implying a crystal-structure evolution from a stratified structure to a quasi-two-dimensional or three-dimensional structure [24,32,55].

IV. CONCLUSIONS

In conclusion, our study provides a comprehensive investigation of the pressure-dependent and layer-dependent interlayer coupling and vibrational properties of NL and bulk $MoTe_2$ ($N = 1 - 5$) using DAC technology and Raman spectroscopy. Through our experimental and computational analyses, we have demonstrated that the pressure-induced blueshift rates of the low-frequency S and LB modes in $MoTe_2$ exhibit layer-dependent behavior, with the blueshift rate increasing and decreasing as the layer number increases, which arises from the layer-dependent restoring forces and interlayer coupling, respectively. Furthermore, we reveal that the intensity changeover between S and LB modes and between $A_1{}'/A^2_{1g}$ and E'/E^1_g modes can be attributed to the pressure-induced enlarged in-plane component of interlayer Te–Te bond compared to out-of-plane component and increase of out-of-plane component of intralayer Mo–Te bond relative to in-plane component, respectively, as supported by the bond-polarization model. Our study demonstrates that $MoTe_2$ retains its layer-dependent properties even under high pressure within a homogeneous crystal structure. This layer-dependent behavior in the low-frequency interlayer vibration modes provides valuable insights into the interlayer coupling and vibrational properties of $MoTe_2$. We anticipate that these phenomena are not exclusive to $MoTe_2$ and that the layer-dependent and pressure-dependent properties can deepen our understanding of interlayer coupling and vibrational properties for van der Waals materials [56].

ACKNOWLEDGMENTS

The research presented in this paper was supported by various funding agencies. The authors would like to acknowledge the generous support of the National Natural Science Foundation of China (Grant No. 52373311), the Hunan Provincial Science Fund for Distinguished Young Scholars (Grant No. 2020JJ2059), the Youth Innovation Team (Grant No. 2019012) of Central South University (CSU), and the Hunan Province Key Research and Development Project (Grant No. 2019GK2233). Financial assistance from the National Natural Science Foundation of China (Grants No. 62090035 and No. U19A2090), the Key Program of the Science and Technology Department of Hunan Province (Grants No. 2019XK2001 and No. 2020XK2001), the Science and Technology Innovation Basic Research Project of Shenzhen (Grant No. JCYJ20190806144418859), the High-Performance Complex Manufacturing Key State Lab Project, and Central South University (Grant No. ZZYJKT2020-12) is also acknowledged. Z.W.L, acknowledges the support of the Australian Research Council (ARC Discovery Project No. DP180102976). J.-T.W. acknowledges the support from the National Key Research and Development Program of China (Grant No. 2020YFA0711502), the Strategic Priority Research Program of the Chinese Academy of Sciences (Grant No. XDB33000000), and the National Natural Science Foundation of China (Grant No. 11974387). The authors acknowledge the High Performance Computing Center of Central South University and the Beijing Super Cloud Computing Center (BSCC) [56] for providing computing resources for this work.

The project management and design were overseen by Y.L. The high-pressure measurements were conducted by X.X. and J.D. The device fabrication, sample preparation, and characterization using Raman and photoluminescence (PL) techniques were performed by X.X., J.D., H.Z., S.L., B.W., and Z.L. Y.L., H.Z., B.W., J.H., and Z.L. contributed to the data interpretation. Theoretical calculations based on density-functional theory (DFT) and related explanations were provided by J.-T.W. The initial drafting of the paper was carried out by Y.L., X.X., J.D., and Z.L. Subsequently, the manuscript underwent a rigorous revision process, in which all authors actively participated and made significant contributions.

The authors declare that they have no competing interests.

[1] A. K. Geim, Graphene: Status and prospects, Science **324**, 1530 (2009).

[2] A. Castellanos-Gomez, Black phosphorus: Narrow gap, wide applications, J. Phys. Chem. Lett. **6**, 4280 (2015).

[3] H. Zeng and X. Cui, An optical spectroscopic study on two-dimensional group-VI transition metal dichalcogenides, Chem. Soc. Rev. **44**, 2629 (2015).

[4] S. L. Li, K. Tsukagoshi, E. Orgiu, and P. Samori, Charge transport and mobility engineering in two-dimensional transition

metal chalcogenide semiconductors, Chem. Soc. Rev. **45**, 118 (2016).

[5] Q. H. Wang, K. Kalantar-Zadeh, A. Kis, J. N. Coleman, and M. S. Strano, Electronics and optoelectronics of two-dimensional transition metal dichalcogenides, Nat. Nanotechnol. **7**, 699 (2012).

[6] M. Wu, Y. Xiao, Y. Zeng, Y. Zhou, X. Zeng, L. Zhang, and W. Liao, Synthesis of two-dimensional transition metal dichalcogenides for electronics and optoelectronics, InfoMat **3**, 362 (2020).

[7] X.-L. Li, W.-P. Han, J.-B. Wu, X.-F. Qiao, J. Zhang, and P.-H. Tan, Layer-number dependent optical properties of 2D materials and their application for thickness determination, Adv. Funct. Mater. **27**, 1604468 (2017).

[8] H. S. Lee, S. W. Min, Y. G. Chang, M. K. Park, T. Nam, H. Kim, J. H. Kim, S. Ryu, and S. Im, MoS_2 nanosheet phototransistors with thickness-modulated optical energy gap, Nano Lett. **12**, 3695 (2012).

[9] G. Cao, Y. An, Q. Bao, and X. Li, Physics and optoelectronic simulation of photodetectors based on 2D materials, Adv. Opt. Mater. **7**, 1900410 (2019).

[10] Y. Liu, C. Zeng, J. Zhong, J. Ding, Z. M. Wang, and Z. Liu, Spintronics in two-dimensional materials, Nanomicro Lett. **12**, 93 (2020).

[11] J. R. Schaibley, H. Yu, G. Clark, P. Rivera, J. S. Ross, K. L. Seyler, W. Yao, and X. Xu, Valleytronics in 2D materials, Nat. Rev. Mater. **1**, 16055 (2016).

[12] L. Li, Y. Yu, G. J. Ye, Q. Ge, X. Ou, H. Wu, D. Feng, X. H. Chen, and Y. Zhang, Black phosphorus field-effect transistors, Nat. Nanotechnol. **9**, 372 (2014).

[13] K. M. McCreary, M. Phillips, H. J. Chuang, D. Wickramaratne, M. Rosenberger, C. S. Hellberg, and B. T. Jonker, Stacking-dependent optical properties in bilayer WSe_2, Nanoscale **14**, 147 (2021).

[14] L. Zhang, Z. Zhang, F. Wu, D. Wang, R. Gogna, S. Hou, K. Watanabe, T. Taniguchi, K. Kulkarni, T. Kuo *et al.*, Twist-angle dependence of moire excitons in $WS_2/MoSe_2$ heterobilayers, Nat. Commun. **11**, 5888 (2020).

[15] J. Shi, Y. Li, Z. Zhang, W. Feng, Q. Wang, S. Ren, J. Zhang, W. Du, X. Wu, X. Sui *et al.*, Twisted-angle-dependent optical behaviors of intralayer excitons and trions in WS_2/WSe_2 heterostructure, ACS Photonics **6**, 3082 (2019).

[16] M. L. Lin, Q. H. Tan, J. B. Wu, X. S. Chen, J. H. Wang, Y. H. Pan, X. Zhang, X. Cong, J. Zhang, W. Ji *et al.*, Moire phonons in twisted bilayer MoS_2, ACS Nano **12**, 8770 (2018).

[17] J. M. Quan, L. Linhart, M. L. Lin, D. H. Lee, J. H. Zhu, C. Y. Wang, W. T. Hsu, J. H. Choi, J. Embley, C. Young *et al.*, Phonon renormalization in reconstructed MoS_2 moire superlattices, Nat. Mater. **20**, 1100 (2021).

[18] S. Pei, Z. Wang, and J. Xia, High pressure studies of 2D materials and heterostructures: A review, Mater. Des. **213**, 110363 (2022).

[19] S. Huang, Y. Lu, F. Wang, Y. Lei, C. Song, J. Zhang, Q. Xing, C. Wang, Y. Xie, L. Mu *et al.*, Layer-dependent pressure effect on the electronic structure of 2D black phosphorus, Phys. Rev. Lett. **127**, 186401 (2021).

[20] Y. Qi, M. A. Sadi, D. Hu, M. Zheng, Z. Wu, Y. Jiang, and Y. P. Chen, Recent progress in strain engineering on van der waals 2D materials: tunable electrical, electrochemical, magnetic, and optical properties, Adv. Mater. **35**, 2205714 (2023).

[21] Y. Yan, C. Jin, J. Wang, T. Qin, F. Li, K. Wang, Y. Han, and C. Gao, Associated lattice and electronic structural evolutions in compressed multilayer ReS_2, J. Phys. Chem. Lett. **8**, 3648 (2017).

[22] M. A. ElGhazali, P. G. Naumov, H. Mirhosseini, V. Süß, L. Müchler, W. Schnelle, C. Felser, and S. A. Medvedev, Pressure-induced superconductivity up to 13.1 K in the pyrite phase of palladium diselenide $PdSe_2$, Phys. Rev. B **96**, 060509(R) (2017).

[23] Z. H. Chi, X. M. Zhao, H. Zhang, A. F. Goncharov, S. S. Lobanov, T. Kagayama, M. Sakata, and X. J. Chen, Pressure-induced metallization of molybdenum disulfide, Phys. Rev. Lett. **113**, 036802 (2014).

[24] Z. Zhao, H. Zhang, H. Yuan, S. Wang, Y. Lin, Q. Zeng, G. Xu, Z. Liu, G. K. Solanki, K. D. Patel *et al.*, Pressure induced metallization with absence of structural transition in layered molybdenum diselenide, Nat. Commun. **6**, 7312 (2015).

[25] J. Xia, J. X. Yan, Z. H. Wang, Y. M. He, Y. J. Gong, W. Q. Chen, T. C. Sum, Z. Liu, P. M. Ajayan, and Z. X. Shen, Strong coupling and pressure engineering in WSe_2-MoSe_2 heterobilayers, Nat. Phys. **17**, 92 (2021).

[26] X. Dou, K. Ding, D. Jiang, and B. Sun, Tuning and identification of interband transitions in monolayer and bilayer molybdenum disulfide using hydrostatic pressure, ACS Nano **8**, 7458 (2014).

[27] Z. Chi, X. Chen, F. Yen, F. Peng, Y. Zhou, J. Zhu, Y. Zhang, X. Liu, C. Lin, S. Chu *et al.*, Superconductivity in pristine $2H_a-MoS_2$ at ultrahigh pressure, Phys. Rev. Lett. **120**, 037002 (2018).

[28] Y. Qi, P. G. Naumov, M. N. Ali, C. R. Rajamathi, W. Schnelle, O. Barkalov, M. Hanfland, S. C. Wu, C. Shekhar, Y. Sun *et al.*, Superconductivity in weyl semimetal candidate $MoTe_2$, Nat. Commun. **7**, 11038 (2016).

[29] X. Fu, F. Li, J.-F. Lin, Y. Gong, X. Huang, Y. Huang, B. Han, Q. Zhou, and T. Cui, Pressure-dependent light emission of charged and neutral excitons in monolayer $MoSe_2$, J. Phys. Chem. Lett. **8**, 3556 (2017).

[30] C. Li, Y. Liu, Q. Yang, Q. Zheng, Z. Yan, J. Han, J. Lin, S. Wang, J. Qi, Y. Liu *et al.*, Tuning of optical behavior in monolayer and bilayer molybdenum disulfide using hydrostatic pressure, J. Phys. Chem. Lett. **13**, 161 (2022).

[31] M. Zhu, Z. Zhang, T. Zhang, D. Liu, H. Zhang, Z. Zhang, Z. Li, Y. Cheng, and W. Huang, Exchange between interlayer and intralayer exciton in WSe_2/WS_2 heterostructure by interlayer coupling engineering, Nano Lett. **22**, 4528 (2022).

[32] A. P. Nayak, Z. Yuan, B. Cao, J. Liu, J. Wu, S. T. Moran, T. Li, D. Akinwande, C. Jin, and J.-F. Lin, Pressure-modulated conductivity, carrier density, and mobility of multilayered tungsten disulfide, ACS Nano **9**, 9117 (2015).

[33] G. Pizzi, S. Milana, A. C. Ferrari, N. Marzari, and M. Gibertini, Shear and breathing modes of layered materials, ACS Nano **15**, 12509 (2021).

[34] A. A. Puretzky, A. D. Oyedele, K. Xiao, A. V. Haglund, B. G. Sumpter, D. Mandrus, D. B. Geohegan, and L. Liang, Anomalous interlayer vibrations in strongly coupled layered $PdSe_2$, 2D Mater. **5**, 035016 (2018).

[35] Q. J. Song, Q. H. Tan, X. Zhang, J. B. Wu, B. W. Sheng, Y. Wan, X. Q. Wang, L. Dai, and P. H. Tan, Physical origin of Davydov splitting and resonant Raman spectroscopy of Davydov

components in multilayer $MoTe_2$, Phys. Rev. B **93**, 115409 (2016).

[36] P. H. Tan, W. P. Han, W. J. Zhao, Z. H. Wu, K. Chang, H. Wang, Y. F. Wang, N. Bonini, N. Marzari, N. Pugno *et al.*, The shear mode of multilayer graphene, Nat. Mater. **11**, 294 (2012).

[37] X. Zhang, W. P. Han, J. B. Wu, S. Milana, Y. Lu, Q. Q. Li, A. C. Ferrari, and P. H. Tan, Raman spectroscopy of shear and layer breathing modes in multilayer MoS_2, Phys. Rev. B **87**, 115413 (2013).

[38] Y. Huang, Y. H. Pan, R. Yang, L. H. Bao, L. Meng, H. L. Luo, Y. Q. Cai, G. D. Liu, W. J. Zhao, Z. Zhou *et al.*, Universal mechanical exfoliation of large-area 2D crystals, Nat. Commun. **11**, 2453 (2020).

[39] S. B. Desai, S. R. Madhvapathy, M. Amani, D. Kiriya, M. Hettick, M. Tosun, Y. Zhou, M. Dubey, J. W. Ager, D. Chrzan *et al.*, Gold-mediated exfoliation of ultralarge optoelectronically-perfect monolayers, Adv. Mater. **28**, 4053 (2016).

[40] P. J. Zomer, M. H. D. Guimarães, J. C. Brant, N. Tombros, and B. J. van Wees, Fast pick up technique for high quality heterostructures of bilayer graphene and hexagonal boron nitride, Appl. Phys. Lett. **105**, 013101 (2014).

[41] C. Zeng, J. Zhong, Y.-P. Wang, J. Yu, L. Cao, Z. Zhao, J. Ding, C. Cong, X. Yue, Z. Liu *et al.*, Observation of split defect-bound excitons in twisted WSe_2/WSe_2 homostructure, Appl. Phys. Lett. **117**, 153103 (2020).

[42] G. Shen, Y. Wang, A. Dewaele, C. Wu, D. E. Fratanduono, J. Eggert, S. Klotz, K. F. Dziubek, P. Loubeyre, O. V. Fat'yanov *et al.*, Toward an international practical pressure scale: A proposal for an IPPS ruby gauge (IPPS-Ruby2020), High Pressure Res. **40**, 299 (2020).

[43] P. E. Blöchl, Projector augmented-wave method, Phys. Rev. B **50**, 17953 (1994).

[44] G. Kresse and J. Furthmüller, Efficient iterative schemes for ab initio total-energy calculations using a plane-wave basis set, Phys. Rev. B **54**, 11169 (1996).

[45] J. P. Perdew, K. Burke, and M. Ernzerhof, Generalized gradient approximation made simple, Phys. Rev. Lett. **77**, 3865 (1996).

[46] M. Yamamoto, S. T. Wang, M. Ni, Y.-F. Lin, S.-L. Li, S. Aikawa, W.-B. Jian, K. Ueno, K. Wakabayashi, and K. Tsukagoshi, Strong enhancement of raman scattering from a bulk-inactive vibrational mode in few-layer $MoTe_2$, ACS Nano **8**, 3895 (2014).

[47] M. Grzeszczyk, K. Gołasa, M. Zinkiewicz, K. Nogajewski, M. R. Molas, M. Potemski, A. Wysmołek, and A. Babiński, Raman scattering of few-layers $MoTe_2$, 2D Mater. **3**, 025010 (2016).

[48] See Supplemental Material at http://link.aps.org/supplemental/10.1103/PhysRevB.108.155302 for pressure,-dependent Raman spectra of 1–5L and bulk $MoTe_2$; the calculation results of pressure-dependent total mass of bulk $MoTe_2$; the wavenumber difference of high-frequency Raman modes under high pressure; and the fitted coefficients and calculated interlayer distances.

[49] S. Guha, J. Menéndez, J. B. Page, and G. B. Adams, Empirical bond polarizability model for fullerenes, Phys. Rev. B **53**, 13106 (1996).

[50] P. Umari, A. Pasquarello, and A. Dal Corso, Raman scattering intensities in α-quartz: A first-principles investigation, Phys. Rev. B **63**, 094305 (2001).

[51] L. Liang, A. A. Puretzky, B. G. Sumpter, and V. Meunier, Interlayer bond polarizability model for stacking-dependent low-frequency Raman scattering in layered materials, Nanoscale **9**, 15340 (2017).

[52] M. Lazzeri and F. Mauri, First-principles calculation of vibrational Raman spectra in large systems: Signature of small rings in crystalline SiO_2, Phys. Rev. Lett. **90**, 036401 (2003).

[53] S. Sugai and T. Ueda, High-pressure Raman spectroscopy in the layered materials $2H-MoS_2$, $2H-MoSe_2$, and $2H-MoTe_2$, Phys. Rev. B **26**, 6554 (1982).

[54] J. Huang, H. Guo, L. Zhou, S. Zhang, L. Tong, R. Saito, T. Yang, and Z. Zhang, First-principles calculations of double resonance Raman spectra for monolayer $MoTe_2$, Phys. Rev. B **105**, 235401 (2022).

[55] X.-M. Zhao, H.-y. Liu, A. F. Goncharov, Z.-W. Zhao, V. V. Struzhkin, H.-K. Mao, A. G. Gavriliuk, and X.-J. Chen, Pressure effect on the electronic, structural, and vibrational properties of layered $2H-MoTe_2$, Phys. Rev. B **99**, 024111 (2019).

[56] BSSC, www.blsc.cn.